Relaxation and hysteresis near Shapiro resonances in a driven spinor condensate

Bertrand Evrard, An Qu, Karina Jiménez-García, Jean Dalibard, Fabrice Gerbier

Relaxation and hysteresis near Shapiro resonances in a driven spinor condensate

Bertrand Evrard, An Qu, Karina Jiménez-García, Jean Dalibard and Fabrice Gerbier

Laboratoire Kastler Brossel, Collège de France, CNRS,
ENS-PSL Research University, Sorbonne Université,
11 Place Marcelin Berthelot, 75005 Paris, France

(Dated: March 29, 2019)

Driving a many-body quantum system in a periodic manner gives access to its fundamental properties, both in terms of energy spectrum and relaxation mechanisms. It also leads to important applications, as shown by Superconducting Josephson Junctions (SCJJs): Thanks to the so-called Shapiro resonances that occur in the presence of a micro-wave drive, SCJJs constitute metrological devices relating the drive frequency to the voltage across the junction. Here we present a detailed experimental study of an atomic analog of a driven SCJJ, based on a spinor Bose-Einstein condensate of sodium atoms. We analyze the short-time evolution of the system in terms of a slow Hamiltonian dynamics, superimposed with a rapid micro-motion. After a long-time evolution, we observe that the system may relax to a non-equilibrium steady state and exhibit a hysteretic behavior. We compare our experimental results with simple phenomenological models of dissipation, that can roughly be described as amplitude or phase damping. We find that the amplitude damping model is able to reproduce quantitatively our observations, while the phase damping model fails qualitatively in certain regimes. Our study therefore constitutes an accurate benchmark for the development of an *ab initio* microscopic theory of the relaxation processes in this driven many-body system.

I. INTRODUCTION

The Josephson effect is the hallmark of macroscopic quantum phenomena in quantum fluids, from superconductors [1–4] to superfluid Helium [5–8], polariton systems [9–11] and ultracold atoms in double-well potentials [12–17]. In all variants, the phase of a macroscopic wave function is controlled by an external bias parameter. In Superconducting Josephson Junctions (SCJJs), a voltage bias determines the relative phase between the two superconducting order parameters on each side of the junction and the supercurrent is proportional to the sine of this phase [1–3]. This leads to some remarkable phenomena, such as the AC Josephson effect where a static voltage generates an oscillating current at the characteristic Josephson frequency ω_0. Conversely, in the "inverse AC Josephson effect" schematized in Fig. 1**a** [2–4], an oscillating voltage $V(t)$ quasi-resonant with ω_0 can carry a DC current across the junction.

In SCJJs, resonances occur when the drive frequency ω fulfills $k\omega = \omega_0$ for integer k [2]. These resonances appear in the form of Shapiro spikes in the voltage-current characteristics of the driven junction at constant bias voltage, or steps at constant bias current [4]. Shapiro steps are at the core of Josephson voltage standards, which are essentially perfect frequency-voltage converters enabled by macroscopic quantum effects [4]. Energy dissipation plays a crucial role in such devices [4]. Indeed without dissipation, the system would not relax towards the exact resonance where the macroscopic phase locks to the drive.

Ultracold atoms exhibit two variants of the Josephson effect. In the first variant ("external Josephson effect"), two superfluids are coupled through a weak link [12–17], in direct analogy with the SCJJs. In the second variant ("internal Josephson effect"), coherent dynamics can oc-cur between internal degrees of freedom [18, 19]. Here we focus on the specific case of spin $F = 1$ atoms, with $m = 0, \pm 1$ the magnetic quantum number labeling the Zeeman components, as illustrated in Fig. 1**b**. An applied magnetic field plays the role of the external bias. The Josephson-like internal dynamics is generated by coherent, spin-changing collisions of the form $2 \times (m = 0) \leftrightarrow (m = +1) + (m = -1)$ instead of single-particle tunneling [20, 21]. Compared to the original SCJJ, cold atoms implementations of the Josephson effect have an important asset when one tries to elucidate the microscopic mechanisms at play in the device: the typical time scales are on the order of milliseconds or longer, enabling a time-resolved study of the dynamics which is difficult to access in superconducting systems, where the microscopic time scales are in the picosecond range.

So far most experimental studies on atomic spinor gases were performed with only a static bias and no modulation [21–32]. The driven case was explored only recently, with experiments demonstrating either the freezing of the evolution by frequent "kicks" in spin space [33], or spin-nematic squeezing near a parametric resonance [34]. In this article, we extend the analogy between SCJJs and atomic spinor gases to the driven regime, where Shapiro resonances occur. Using a spin-1 Bose–Einstein condensate (BEC) of sodium atoms, we observe such resonances (see Fig. 1**c**) and characterize them in the non-linear regime, where the phase dynamics is not solely controlled by the external static bias. We study the coherent dynamics at short times and the relaxation at long times (tens of seconds, corresponding to tens of thousands of the drive oscillation period). Near resonance, in the strongly driven regime, we find that the driven BEC relaxes to asymptotic states that are not stable without drive (Fig. 1**c**). In this sense, our sys-
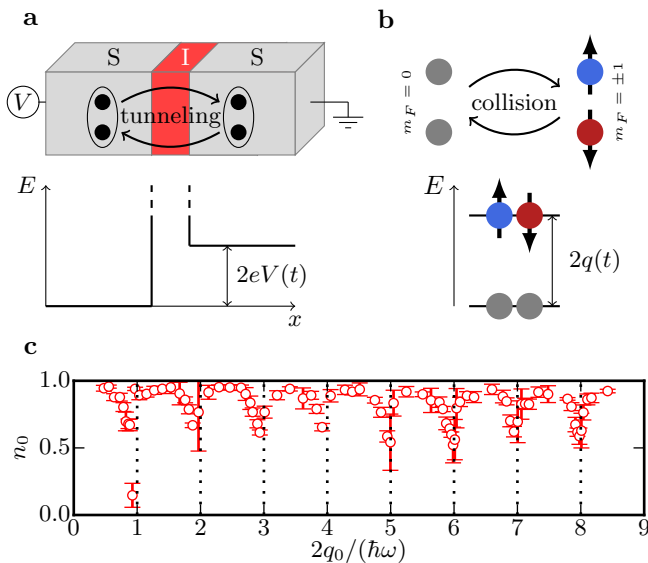
FIG. 1. Analogy between two physical systems exhibiting macroscopic quantum coherence: a superconducting Josephson junction (SCJJ–**a**) and a spin-1 atomic Bose-Einstein condensate (BEC–**b**). For SCJJs (respectively, BECs), tunneling through the barrier (resp., spin-mixing interactions) generates an electric current (resp., a spin current) controlled by the relative phase across the barrier (resp., between the Zeeman components of the spin-1 wave function). An external energy bias $E(t)$ controls the rate of change of the relative phase: the electrostatic energy $E(t) = 2eV(t)$ for SCJJs, with V the voltage and $2e$ the charge of a Cooper pair, and the quadratic Zeeman energy $E(t) = 2q(t)$ of a pair of $m = \pm 1$ atoms for spin-1 BECs. If the energy bias is modulated around a static value E_0, a Shapiro resonance occurs when the modulation frequency ω fulfills the resonance condition $k_0 \hbar \omega = E_0$, with k_0 a positive integer. **c**: Observation of several ($k_0 = 1 - 8$) Shapiro resonances in a spin-1 atomic condensate after a relaxation time of 30 s. Here, n_0 is the reduced population of the $m = 0$ Zeeman state, and q_0 is the static QZE. The experiment was performed with a sodium Bose-Einstein condensate containing $N \approx 2 \cdot 10^4$ atoms, with a magnetization per atom $m_{||} = 0$. We varied q_0 for a fixed drive frequency $\omega / 2\pi = 100$ Hz.

tem constitutes a many-body version of the celebrated Kapitza pendulum [35–37]. The stationary states correspond to phase-locked solutions of the Josephson equation, generalized to include dissipation and analogous to the stationary states of driven SCJJs [4].

In our experiments, dissipation presumably results from interactions between condensed and noncondensed atoms that lead to damping of coherent macroscopic phenomena and thermalization. Thermalization of driven quantum systems has been studied intensely in the past few years [38–40]. The general expectation is that energy is absorbed from the drive, eventually heating to infinite temperatures [41–43]. However, the heating time scale τ_h can become extremely long. Rigorous proofs are only available for high-frequency modulation and systems with a bounded spectrum: Refs. [44–46] have shown that $\tau_h = e^{\mathcal{O}(\omega/\Delta)}$, with Δ^{-1} the faster intrinsic timescale of the non-driven system and $\omega \gg \Delta$ the modulation frequency. For times $t \ll \tau_h$, the system may attain a pre-thermalized "Floquet-Gibbs" state corresponding to the equilibrium state of an effective, secular Hamiltonian. In this work we use near-resonant modulation and probe a system with an *a priori* unbounded spectrum [47]. We observe a long-time steady state that differs from both the infinite temperature state and a Floquet-Gibbs state associated with the secular Hamiltonian.

We introduce in this article a phenomenological model obtained by adding a suitable dissipative term to the coherent, Josephson-like equations describing the spinor dynamics. We compare its predictions with those of a former model used in the literature to describe relaxation in atomic Josephson-like settings. These two models can be roughly classified as amplitude or phase damping, respectively. Their predictions are barely distinguishable from each other without driving but differ spectacularly in the strongly driven case. More precisely, the "phase-damping model" proposed in [26], is clearly incompatible with the experimental observations, whereas our "amplitude-damping model" agrees quantitatively with them. This suggests that our experimental results can be used as a benchmark for *ab initio* theories of a driven many-body system, as they constrain strongly the form of damping prevailing in experiments.

The paper is organized as follows. In Section II, we review the main features of our experiment and of the theoretical description of spinor condensates. We highlight the analogies and differences with Josephson physics in superconducting junctions. We also discuss for later reference spin-mixing oscillations without driving, highlighting both the coherent features [22–28] and the dissipative aspects [26]. In Section III, we turn to the driven system and characterize experimentally and theoretically the non-linear secular dynamics in the vicinity of the resonance. Measuring both the Zeeman population and the relative phase of the atoms, we identify two regimes, an "oscillating regime" where the atomic phase is locked to the drive, and a "rotating regime" where the atomic phase runs independently from the drive. In Section IV, we study the relaxation of the driven spin-1 BEC for long evolution times. In a narrow frequency window around each Shapiro resonance, we observe relaxation to a non-equilibrium steady state that has no analog in the non-driven system. We also show that the system displays hysteresis when the drive frequency is scanned accross a Shapiro resonance. Finally, we conclude and draw some perspectives of this work in Section V.

II. SPIN-MIXING OSCILLATIONS

This section is devoted to the theoretical modelling of a spinor Bose–Einstein condensate, as well as its experimental implementation and characterization. We first fo-

cus on the coherent dynamics of the system in the mean-field and single mode approximations, and we show that it can be viewed as a classical one-dimensional Hamiltonian system. Here the relevant canonically conjugate variables are n_0 and θ, where n_0 is the population of the $m = 0$ Zeeman state, and θ a particular combination of the phase of the three Zeeman states. We emphasize the deep analogies that exist between the equations of motion of the spinor gas and those of a driven SCJJ, with n_0 playing the role of the supercurrent and θ the role of the phase difference across the junction. We then present our experimental setup and explain how we access these two relevant variables n_0 and θ. Finally, we describe two simple models for the relaxation of the dynamics of the spinor BEC. In particular, we show experimental results that indicate that in the non-driven case, it is not possible to discriminate between these two relaxation models.

A. Coherent dynamic of spinor condensates

1. Relevant contributions to the energy

We consider spin $F = 1$ atoms immersed in a spatially uniform magnetic field $\boldsymbol{B} = B\boldsymbol{u}$, where the orientation $\boldsymbol{u}$ is taken as quantization axis. The atoms can occupy all three Zeeman states $|F, m\rangle_{\boldsymbol{u}}$, where $m = 0, \pm 1$ refers to the eigenvalue of $\hat{\boldsymbol{f}} \cdot \boldsymbol{u}$ and where $\hat{f}_{x,y,z}$ are the spin-1 matrices.

As for most magnetic materials, the dynamics and equilibrium properties of spinor condensates are governed by (i) the Zeeman energy $\sim \mu_{\mathrm{B}}B$ in the applied magnetic field, where μ_{B} is the Bohr magneton, and (ii) the spin-dependent interactions. In this work, the direction of the applied magnetic field varies in time, but only on a time scale much longer than the Larmor period $h/\mu_{\mathrm{B}}B$. The single-particle spin states then follow adiabatically the changes of the direction of $\boldsymbol{B}(t)$ (see Appendix A for more details). For relatively low values of B, the Zeeman energy of a single atom is thus given by

$$\hat{h}_{\mathrm{Z}} = p(t)\hat{f}_z + q(t)\left[\hat{f}_z^2 - 1\right] + \mathcal{O}(B^3). \qquad (1)$$

In this expression, the linear Zeeman term proportional to $p(t) = g_F \mu_{\mathrm{B}} B(t)$ ($g_F = -1/2$ the Landé factor) is essentially the contribution of the spin of the valence electron, and the quadratic Zeeman energy (QZE) proportional to $q(t) = \alpha_q \boldsymbol{B}^2$ (with $\alpha_q \approx h \times 277\,\mathrm{Hz/G^2}$ for sodium atoms) gives the first correction due to the nuclear spin [19].

Interactions between alkali atoms are mainly due to short-range van der Waals interactions. Magnetic dipole-dipole interactions are usually much weaker [48]. Neglecting the latter, the interaction potential between two atoms is invariant under spin rotations. On the other hand, the Zeeman term is invariant only by rotations around the quantization axis $\boldsymbol{u}$, which thus constitutes the symmetry axis of the problem. For a many-atom system, this symmetry implies that the longitudinal magnetization per atom, $m_{||} = \langle \hat{\boldsymbol{F}} \cdot \boldsymbol{u}\rangle/N$, with $\hat{\boldsymbol{F}}$ the total spin operator and N the total atom number, is a conserved quantity [19, 20, 22]. The linear Zeeman energy, proportional to $m_{||}$, can then be eliminated without loss of generality by transforming to a frame rotating around the quantization axis $\boldsymbol{u}$ at the Larmor frequency (see Sec. II A 2). The Zeeman energy then reduces to the QZE alone, $\hat{h}_{\mathrm{Z}} = q(t)\left[\hat{f}_z^2 - 1\right] + \mathcal{O}(B^3)$.

2. Single-mode regime

We focus in this work on the so-called *single-mode regime* of spinor condensates [20, 49, 50]. This regime is realized for a condensate confined in a tight trap, such that spin excitations correspond to energies much lower than the confinement energy associated with the spatial variations of the wave function. In this situation, the lowest energy states correspond to various spin states, but to the same single-mode spatial orbital $\bar{\phi}(\mathbf{r})$. It is convenient to use a second-quantized notation and to introduce the operator $\hat{a}_m$ annihilating a boson in the single-particle state $|F, m\rangle_{\boldsymbol{u}} \otimes |\bar{\phi}\rangle$. The spin physics is then described by an effective low-energy spin Hamiltonian [19, 51],

$$\hat{H}_{\mathrm{s}} = \frac{U_{\mathrm{s}}}{2N}\hat{\boldsymbol{F}}^2 - q\hat{N}_0. \qquad (2)$$

Here N is the total atom number, U_{s} is a spin-dependent interaction energy determined by the single-mode orbital, $U_{\mathrm{s}} = (4\pi\hbar^2 N a_s)/m_{\mathrm{Na}} \times \int |\bar{\phi}(\boldsymbol{r})|^4\,\mathrm{d}^3r$, with $a_s \approx 0.13\,\mathrm{nm}$ the spin-dependent scattering length [52] and m_{Na} the mass of a sodium atom. The QZE is proportional to q and to the operator $\hat{N}_0 = \hat{a}_0^\dagger \hat{a}_0$ counting the population in the Zeeman state $m = 0$. The procedure for calibrating U_{s} is described in Appendix B. Note that by construction the Hamiltonian in Eq. (2) is valid only at low energies. In particular, it cannot describe the noncondensed modes involving orbital degrees of freedom other than $\bar{\phi}(\mathbf{r})$.

In the single-mode regime, almost all atoms condense at low temperature into the same single-particle state $\boldsymbol{\Psi} = \boldsymbol{\zeta} \otimes \bar{\phi}(\boldsymbol{r})$, with $\boldsymbol{\zeta}$ a complex vector independent of space. The components $\zeta_m = \sqrt{n_m}e^{i\phi_m}$, where n_m is the fractional (normalized to the total atom number) population of the Zeeman state m, are not independent. Accounting for (i) an overall normalization, (ii) an irrelevant global phase, and (iii) the conservation of magnetization leaves only three independent real variables. A convenient choice for these variables are the relative population n_0 of the $m = 0$ state and the two relative phases

$$\theta = \phi_{+1} + \phi_{-1} - 2\phi_0, \quad \eta = \phi_{+1} - \phi_{-1}. \qquad (3)$$

The rate of change $\hbar\dot{\theta}$ can be interpreted as a chemical potential difference driving the "reaction" $(m =$

+1) + (m = −1) ↔ 2 × (m = 0), with a "chemical equilibrium" reached for $\theta = 0$ or π (see Eq. (9) below). The phase η would describe the Larmor precession due to the linear Zeeman term in the original Zeeman Hamiltonian. The transformation $\zeta_m \to \zeta_m e^{-i\frac{mpt}{\hbar}}$ to a frame rotating at the Larmor frequency around the quantization axis $\boldsymbol{u}$ removes the contribution $\propto p$ to the Zeeman Hamiltonian, without loss of generality.

In this work, we focus on the case $m_{||} = 0$, so that $n_{+1} = n_{-1}$. The spin energy for a condensate in the state $\boldsymbol{\Psi}$ is then

$$E_{\mathrm{s}}(n_0, \theta, t) = U_{\mathrm{s}} n_0 (1 - n_0)(1 + \cos\theta) - q(t) n_0. \quad (4)$$

Note that this energy does not depend on the phase η. For a static QZE $q > 0$ and antiferromagnetic interactions $U_{\mathrm{s}} > 0$, it is minimal for the so-called polar state [53] with $n_0 = 1$ that minimizes separately the Zeeman and interaction terms in Eq. (4).

3. Spin-mixing oscillations and Josephson physics

The equations of motion for a spin-1 BEC in the single mode approximation can be derived from the Gross-Pitaevskii energy functional (see [19] and references therein). We start with the dynamical part of the Lagrangian for the Schrödinger equation $i\hbar \int \boldsymbol{\Psi}^* \cdot \dot{\boldsymbol{\Psi}}$ and expresses it in terms of the spin variables. Subtracting the Zeeman and interaction energies (4), we obtain the Lagrangian for $m_{||} = 0$,

$$\mathcal{L}(n_0, \theta, \dot{\theta}, t) = \frac{\hbar}{2} n_0 \dot{\theta} - E_{\mathrm{s}}(n_0, \theta, t). \quad (5)$$

The two Euler–Lagrange equations for n_0 and θ

$$\frac{\mathrm{d}}{\mathrm{dt}} \frac{\partial \mathcal{L}}{\partial \dot{\theta}} = \frac{\partial \mathcal{L}}{\partial \theta}, \qquad \frac{\mathrm{d}}{\mathrm{dt}} \frac{\partial \mathcal{L}}{\partial \dot{n}_0} = \frac{\partial \mathcal{L}}{\partial n_0}, \quad (6)$$

read in this particular case

$$\frac{\hbar}{2} \dot{n}_0 = -\frac{\partial E_{\mathrm{s}}}{\partial \theta}, \qquad \frac{\hbar}{2} \dot{\theta} = \frac{\partial E_{\mathrm{s}}}{\partial n_0}. \quad (7)$$

The explicit form of these equations of motion is thus [21]

$$\hbar \dot{n}_0 = 2U_{\mathrm{s}} n_0 (1 - n_0) \sin\theta, \quad (8)$$

$$\hbar \dot{\theta} = -2q(t) + 2U_{\mathrm{s}}(1 - 2n_0)(1 + \cos\theta). \quad (9)$$

For this choice of the Lagrange function, the conjugate momentum of the phase θ is

$$p_\theta \equiv \frac{\partial \mathcal{L}}{\partial \dot{\theta}} = \frac{\hbar}{2} n_0, \quad (10)$$

The Hamilton formulation of the dynamics corresponds therefore to a one-dimensional system, with the classical Hamiltonian $\mathcal{H} = p_\theta \dot{\theta} - \mathcal{L}$ defined as

$$\mathcal{H}(p_\theta, \theta, t) \equiv E_{\mathrm{s}}(n_0 = 2p_\theta/\hbar, \theta, t). \quad (11)$$

The corresponding Hamilton–Jacobi equations are identical to Eq. (7). Note that in this formulation, E_{s} represents the *total* energy (kinetic plus potential) of the one-dimensional system.

Eqs. (8,9) contain the two main ingredients for Josephson physics [18]. Consider first Eq. (8): the "spin current" $\dot{n}_0$ is generated by *coherent* spin-mixing interaction processes controlled by the phase θ. This is analogous to the celebrated Josephson relation $I_s \propto \sin\phi$ linking the supercurrent I_s in a SCJJ to the relative phase ϕ between the two superconductors on each side of the junction. The additional factor $n_0(1 - n_0)$ enforces that the population n_0 stays in the interval $[0, 1]$ and thus simply corresponds to a slowing down of the dynamics when the BEC reaches one of the extreme points $n_0 = 0$ or $n_0 = 1$.

Consider now the second equation of motion Eq. (9): the external bias $q(t)$ –analogous to the voltage drop $V(t)$ across the junction– controls the rate of change $\dot{\theta}$ of the relative phase. This is analogous to the second Josephson relation $\hbar\dot{\phi} = 2eV$ with $2e$ the charge of a Cooper pair. Here, we also find an additional term [the last term of Eq. (9)], which describes how interactions can alter the resonance and the dynamics of the phase.

To summarize, the equations of motion describing the coherent dynamics of a driven spinor condensate present a deep analogy with those of a driven SCJJ, with identical dominant contributions. There exist however differences between Eqs. (8,9) and the "standard" Josephson relations, which essentially reflect the fact that these gases can be viewed as closed interacting systems; therefore Josephson-like phenomena typically lead, in the present case, to population oscillations of large amplitude (comparable to the total atom number), and not to a steady current as for superconducting circuits connected to charge reservoirs.

B. Experimental setup and protocol

In this paper, we focus on the situation where the static bias $q_0/h \sim 300\,\mathrm{Hz}$ is much larger than $U_{\mathrm{s}}/h \sim 30\,\mathrm{Hz}$. We present in this subsection the experimental protocol from which we infer the relevant variables n_0 and θ, and we illustrate it on the static case, *i.e.*, when $q = q_0$ is constant in time. In the regime $q_0 \gg U_{\mathrm{s}}$ (called Zeeman regime in [23]), the QZE determines the phase evolution up to small corrections, $\theta(t) \approx \theta(0) - 2q_0 t/\hbar$. Eq. (8) then predicts harmonic oscillations of n_0 at the frequency $\approx 2q_0/\hbar$, with a small amplitude $\propto U_{\mathrm{s}}/q_0$ [21–25]. These oscillations constitute the analogue for spinor gases of the AC-Josephson effect: a constant DC bias induces a periodic AC current.

1. Condensate preparation

In order to observe experimentally the AC spin oscillations induced by a static bias q_0, we prepare a quasi-pure
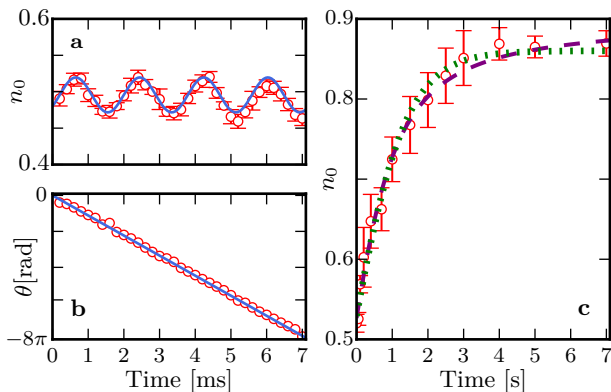
FIG. 2. **a-b**: Spin-mixing oscillations without driving in the Zeeman regime $q_0 \gg U_s$. The time evolution of the population n_0 in (**a**) and the relative phase θ in (**b**.). **c**: Relaxation of n_0 at long times. The red points correspond to the experimental data and the lines show the fit results for the two dissipative models DM 1 (dotted green line) and DM 2 (dashed purple line) introduced in Sec. II C 2. The values of the fit parameters are given in Sec. II C 3.

condensate of spin-1 sodium atoms in a crossed optical dipole trap. The condensate contains $N \approx 10^4$ atoms, with a condensed fraction $\gtrsim 0.9$. The condensate is initially polarized in the $m = +1$ state (except in Section IV D). Our main observables are the relative populations n_m of the Zeeman sublevels $m = 0, \pm 1$. We measure these populations using absorption imaging after a time-of-flight in a magnetic field gradient separating the different Zeeman components ("Stern-Gerlach imaging"). The experimental setup, preparation steps and Stern-Gerlach imaging were described in details in our previous publications [54, 55].

In the experiments described in the following, we initiate spin-mixing dynamics by rotating the internal state of the spin-polarized BEC. This spin rotation is the only exception to the adiabaticity condition indicated above. Experimentally, we apply a radiofrequency field resonant at the Larmor frequency for a time $t_{\pi/2} \approx 40\,\mu s$, resulting in a rotation by an angle of $\pi/2$ around an axis orthogonal to the quantization axis $\boldsymbol{u}$. With the Zeeman state $|m = +1\rangle$ as starting point, the internal state after rotation is $\frac{1}{2}\left(|m = +1\rangle + |m = -1\rangle\right) + \frac{1}{\sqrt{2}}|m = 0\rangle$. Hence the initial $m = 0$ population and longitudinal magnetization are respectively $n_{0,i} = 1/2$ and a $m_{||} = 0$.

2. Measurement of the phase θ

The spin-mixing dynamics is characterized by oscillations of both the population n_0 and the phase θ. The Stern–Gerlach imaging procedure mentioned above readily provides the value of n_0. An example is given in Fig. 2**a**, which shows the expected sinusoidal evolution of $n_0(t)$ in the non-driven case. We use the method in-

troduced in [55] to measure the phase θ. This method relies on the fact that the orientation of the transverse magnetization per atom $\boldsymbol{m}_\perp$ (controlled by the phase η, see Section II A) varies randomly for each realization of the experiment. Indeed, the spin energy E_s depends only on the magnitude of $\boldsymbol{m}_\perp$ but not on its orientation. After averaging over many realizations, the distribution of $\boldsymbol{m}_\perp$ has a zero mean but a non-zero variance,

$$\langle m_\perp^2 \rangle = 2n_0(1 - n_0)(1 + \cos\theta), \tag{12}$$

that depends explicitly on $\cos\theta$. Here $\langle \cdot \rangle$ denotes a statistical average over the realizations.

In practice, we apply a radio-frequency pulse to induce a spin rotation of $\pi/2$ around the y axis and measure the magnetization $m'_{||}$ after rotation. We repeat the experiment typically $N_{\mathrm{mes}} = 10 - 20$ times and calculate the variance $\langle m'^2_{||} \rangle$ of the experimental results. Using $\langle m'^2_{||} \rangle = \langle m_\perp^2 \rangle / 2 + \mathcal{O}(1/N_{\mathrm{mes}})$, we infer the value of $\cos\theta$. In order to determine unambiguously the phase θ itself, we assume that θ wraps monotonically around the unit circle to obtain the illustrative result shown in Fig. 2**b**.

C. Relaxation of spin-mixing oscillations

1. Experimental observation of a dissipative behavior

In the non-driven case, we observe experimentally that for long evolution times, the spin-mixing oscillations are damped and the population $n_0(t)$ eventually relaxes to the expected equilibrium value $n_0 \approx 1$. An exemple of this dissipative behavior is shown in Fig. 2**c**. The characteristic time scale is a few seconds, to be contrasted with the millisecond time scale of the coherent oscillations shown in Fig. 2**a**.

This relaxation, first observed in [26], corresponds to a *loss of energy* of the spinor BEC. Eqs. (8,9) describe a Hamiltonian dynamics where the energy $E_s(n_0, \theta)$ is a constant of motion [21]. As a result, a point or an orbit of the classical phase space (n_0, θ) cannot be attractive, and relaxation cannot occur within this framework. However, experimental systems are never perfectly isolated, and their coupling to (many) other degrees of freedom playing the role of an energy reservoir enables energy dissipation and thermalization. In experiments with ultracold atoms, noncondensed particles forming a bath of collective excitations are inevitably present at non-zero temperature and constitute a primary candidate to explain relaxation. We expect that the interaction of the BEC with this bath acts to restore thermodynamic equilibrium, *i.e.* a BEC with all atoms in $m = 0$ for $q_0 > 0$, with a small decrease of the condensed fraction f_c. This is indeed what we observe in Fig. 2c, with a typical relaxation time ($\sim 1\,\mathrm{s}$) that depends on q_0 [26].

2. Phenomenological modelling of the dissipation

An *ab initio* theoretical description of the thermalization dynamics in a spinor BEC would require to go beyond the Bogoliubov [51, 56, 57] or classical field [39] descriptions that are only applicable at short times. In this work, we study relaxation over several seconds, *i.e.* several hundred/thousands times the intrinsic time scales $h/U_s \sim 30\,\mathrm{ms}$ and $h/2q_0 \sim 1\,\mathrm{ms}$ set by interactions and QZE, respectively. To the best of our knowledge, no general framework is available to describe strongly out-of-equilibrium dynamics for single-component gases, let alone spin-1 systems.

Therefore, in order to describe the experimental observations and gain some insight on the dynamics, we take in this work a phenomenological approach. Following [13, 17, 26, 58], we add "by hand" a dissipative term to the coherent spin-mixing equations of motions Eqs. (8,9):

$$\dot{n}_0 = \dot{n}_0|_{\mathrm{coh}} + \dot{n}_0|_{\mathrm{diss}}, \tag{13}$$

$$\dot{\theta} = \dot{\theta}\Big|_{\mathrm{coh}} + \dot{\theta}\Big|_{\mathrm{diss}}. \tag{14}$$

The first dissipative model (DM 1) that we consider was originally proposed in Ref. [26],

$$\mathrm{DM\,1}: \dot{n}_0|_{\mathrm{diss}} = 0, \quad \dot{\theta}_0\Big|_{\mathrm{diss}} = \beta_1 \dot{n}_0. \tag{15}$$

Liu *et al.* argue that the dissipative term in Eq. (15) is the only term linear in $n_0, \theta, \dot{n}_0$ or $\dot{\theta}$ that can explain their measurements [26]. Anticipating on the results in the driven case that will be presented later, we have found that the dissipative model 1 can reproduce our experimental results without driving, but fails to predict the observed steady state in the strongly driven case. This motivated us to explore other dissipative models, not necessarily linear in n_0, θ or their derivatives. We propose in this article the alternative

$$\mathrm{DM\,2}: \dot{n}_0|_{\mathrm{diss}} = -\beta_2 n_0 (1 - n_0)\dot{\theta}, \quad \dot{\theta}_0\Big|_{\mathrm{diss}} = 0. \tag{16}$$

In the context of cold atoms, similar dissipative terms have been proposed [13, 17, 58], mainly in analogy with those describing Ohmic dissipation in SCJJs. The DM 1 corresponds to a resistor connected in series with the junction, and the DM 2 to a resistor in parallel with the junction ("resistively shunted junction model"). The dimensionless phenomenological constants β_1, β_2 are real numbers, which are chosen positive to ensure that the energy E_s always decreases. Indeed, the dissipated power reads for a time-independent QZE

$$\mathcal{P}_{\mathrm{diss}} = \frac{\mathrm{d}E_s}{\mathrm{d}t} = \dot{n}_0|_{\mathrm{diss}} \frac{\partial E_s}{\partial n_0} + \dot{\theta}\Big|_{\mathrm{diss}} \frac{\partial E_s}{\partial \theta} \tag{17}$$

which simplifies into $\mathcal{P}_{\mathrm{diss}}^{(1)} = -\frac{\hbar}{2}\beta_1 \dot{n}_0^2$ for DM 1 and $\mathcal{P}_{\mathrm{diss}}^{(2)} = -\frac{\hbar}{2}\beta_2 n_0 (1 - n_0)\dot{\theta}^2$ for DM 2. In both cases we find energy dissipation provided that the phenomenological damping coefficients $\beta_{1/2} \geq 0$.

3. Relaxation in the non-driven case

For long times, the population n_0 displays oscillations on top of a slowly varying envelope $\bar{\bar{n}}_0$, where the double bar denotes a coarse-grained average over a time long compared to the period of the spin-mixing oscillation $h/(2q_0)$, but short compared to the relaxation time $\tau_{1/2}$. In Appendix C), we show that the solution of the DM 1 is well approximated at long time by

$$\mathrm{DM\,1}: \bar{\bar{n}}_0 \approx 1 - \frac{\tau_1}{t}, \tag{18}$$

with $\tau_1 = \hbar q_0/(\beta_1 U_s^2)$. The DM 2 predicts

$$\mathrm{DM\,2}: \bar{\bar{n}}_0 = \frac{n_{0,\mathrm{i}}}{n_{0,\mathrm{i}} + (1 - n_{0,\mathrm{i}})e^{-t/\tau_2}}, \tag{19}$$

with $\tau_2 = 2\hbar/(\beta_2 q_0)$. Here $n_{0,\mathrm{i}}$ is the initial value of n_0.

We have compared the predictions of the two models to the experimental results shown in Fig. 2c. For this comparison, we account for a small but non-zero thermal fraction. The measured population in $m = 0$ can be written

$$n_0 = f_c n_{0,c} + n_0', \tag{20}$$

with $n_{0,c} = N_{0,c}/N_c$ (resp. n_0') the fraction of condensed (resp. noncondensed) atoms in $m = 0$. Here $N_{m,c}$ denotes the population of condensed atoms in the m state, $N_c = \sum_m N_{m,c}$ the number of condensed atoms, $f_c = N_c/N$ the condensed fraction and N the total atom number. We assume for simplicity that thermal atoms are distributed equally among all Zeeman sublevels, so that $n_0' = (1 - f_c)/3$.

We use Eq. (20) in combination with the dissipative models 1 or 2 for $n_{0,c}$ to fit the experimental data in Fig. 2c, using f_c and the relaxation times $\tau_{1/2}$ as free parameters. We find comparable best-fit parameters for both models : $f_c \approx 0.85(2)$, $\tau_1 \approx 0.18(2)\,\mathrm{s}$ for DM 1, $f_c \approx 0.80(2)$, $\tau_2 \approx 0.86(10)\,\mathrm{s}$ for DM 2. The corresponding phenomenological damping parameters are $\beta_1 \approx 0.20(2)$ and $\beta_2 \approx 1.30(15) \times 10^{-3}$. The two dissipative models fit well our measurements in Fig. 2c, with a small difference that appears at long times, but which is not statistically significant. We conclude that discriminating between the two models is difficult in the non-driven case. We will see later in the article that this is no longer the case in the driven case, where the differences are spectacular at long times.

III. NON-LINEAR SHAPIRO RESONANCES

We now turn to the main topic of this paper, where a sinusoidal modulation of the QZE with frequency ω drives the spinor dynamics. We are interested in the case where $\hbar\omega$ and q_0 are comparable, allowing for a resonant behavior of the system (Sec. III A). We focus in

this section on the short-time dynamics, where the effect of dissipation is negligible. In Sec. III B, we model the evolution close to a resonance by secular equations of motion, which depend on two time-averaged variables $\overline{n}_0$ and ϕ. The quantity $\overline{n}_0$ is the average of the population n_0 over the time period $2\pi/\omega$. The definition of the secular phase ϕ is more involved and will be made explicit in Sec. III B. We then explain how to access experimentally the value of ϕ (Sec. III C). We finally show that our experimental results in this short-time regime are in excellent agreement with the prediction of the secular equations (Sec. III D).

A. Observation of Shapiro resonances

In all what follows we use a sinusoidal modulation of the QZE around a bias value q_0 according to

$$q(t) = q_0 + \Delta q \sin(\omega t + \varphi_{\mathrm{mod}})\,\Theta(t), \qquad (21)$$

with $\Theta(t)$ the Heaviside step function. Experimentally, the x component B_x of the magnetic field is static, and the y component $B_y = \Delta B \cos[(\omega t + \varphi_{\mathrm{mod}})/2 + \pi/4]\,\Theta(t)$ is modulated in a sinusoidal fashion. The QZE is given by Eq. (21) with $q_0 = \alpha_q(B_x^2 + \Delta B^2/2)$ and $\Delta q = \alpha_q \Delta B^2/2$.

In a perturbative picture, spin-mixing resonances occur when a pair of atoms in $m = 0$ can be resonantly transferred to a pair $m = \pm 1$ by absorbing an integer number k of modulation quanta, i.e. when $k\hbar\omega = 2q_0$. We define the detuning by

$$\hbar\delta = 2q_0 - k_0\hbar\omega, \qquad (22)$$

with k_0 the closest integer to $2q_0/(\hbar\omega)$.

The left column of Fig. 3 shows how the population n_0 evolves in time for several values of the modulation frequency ω close to the first resonance with $k_0 = 1$, such that $\delta \ll q_0$. The dynamics of n_0 can be described as the combination of (i) a fast (frequency $\omega \simeq 2q_0/\hbar$) micromotion with a small amplitude, visible in the inset of Fig. 3a1, and (ii) a slow oscillation with a large amplitude. The period of the slow oscillation is a hundred milliseconds or more, much longer than the intrinsic timescales set by the drive period, the QZE or the spin-dependent interactions. This slow dynamics is the result of the coherent build-up over hundreds of periods of the micromotion. The slow "Shapiro oscillations" observed near resonance can be viewed as the counterpart for our closed system of the DC current observed near Shapiro resonances in modulated SCJJs.

Fig. 4 shows the generic behavior observed for longer times, where we observe (i) a damping of the contrast of the oscillations on a time scale of several hundred milliseconds, and (ii) a drift of the baseline value of n_0 towards the equilibrium value without driving, $n_0 = 1$. We attribute the damping (i) mainly to fluctuations of the experimental parameters, leading to shot-to-shot fluctuations of the period and amplitude of the oscillations and
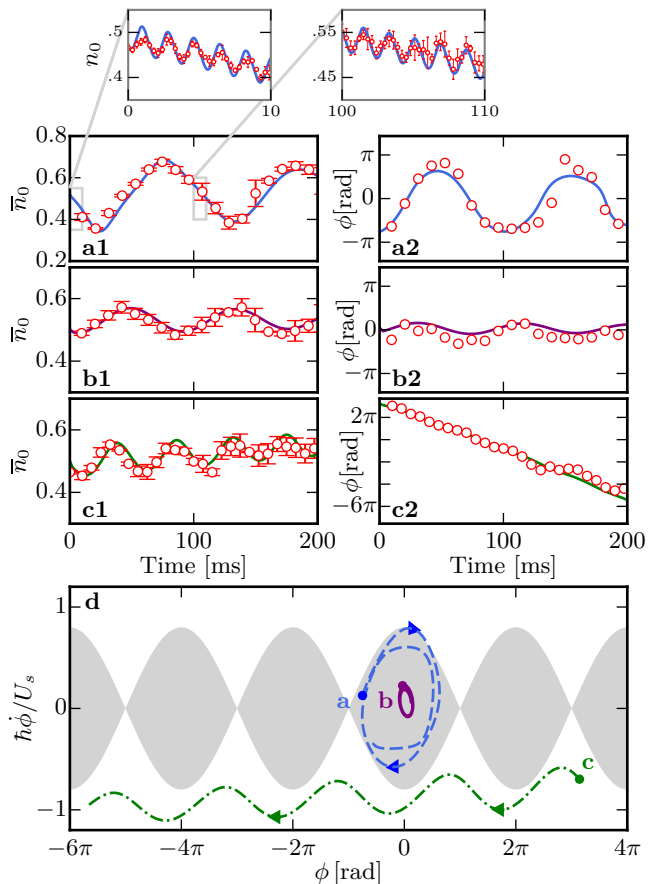

FIG. 3. Observation of secular oscillations near the first Shapiro resonance $k_0 = 1$. We show the relative population $\overline{n}_0$ (**a-c1**) and phase ϕ (**a-c2**) versus time. The parameters in **a1-2**,**b1-2** correspond to the oscillating regime of the pendulum model, while **c1-2** correspond to the clockwise-rotating regime. The lines show the numerical solutions of the dissipative model 2 [Eq. (16)] with $\beta_2 = 1.3 \cdot 10^{-3}$. The calculated curves are further averaged to account for experimental fluctuations of U_{s} (see text). The last panel **d** shows a phase-space portrait of the trajectories in the $(\phi, \dot{\phi})$ plane, with $\dot{\phi}$ calculated from Eq.(24). The dashed blue, solid purple and dashed-dotted green line correspond to **a1-2**, **b1-2** and **c1-2**, respectively. The shaded area covers the phase-space region explored in the oscillating regime of the pendulum model. In the main panels, the observation times are integer multiple of the modulation period $T = 2\pi/\omega$. The data are thus a stroboscopic observation of the secular dynamics, free of the additional micromotion. The two insets in **a1** (with a smaller time sampling) show the micromotion around the main secular oscillation. The static bias is $q_0/h = 276\,\mathrm{Hz}$, the modulation amplitude $\Delta q/h = 43.6\,\mathrm{Hz}$ ($\kappa \simeq 0.08$), and $U_{\mathrm{s}}/h \approx 30\,\mathrm{Hz}$. The detuning is $\delta/2\pi = -5.7\,\mathrm{Hz}$ (**a1-2**,**b1-2**) and $18\,\mathrm{Hz}$ (**c1-2**). For curves **b1-2**, we varied the initial phase (see text) to be in the harmonic regime: $\theta(0) = -0.5(2)\,\mathrm{rad}$ for **a1-2**,**c1-2** and $1.45(2)\,\mathrm{rad}$ for **b1-2**.
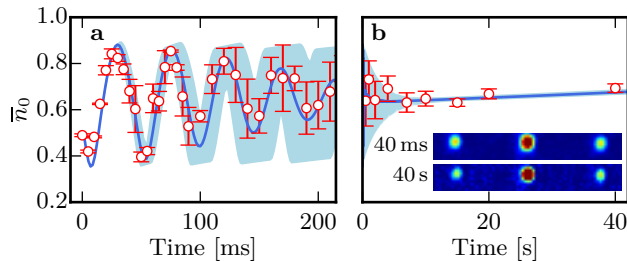
FIG. 4. **a**: Damping of Shapiro oscillations. The solid blue curve is calculated from the dissipative model 2 (DM 2) and averaged over the fluctuations of U_s caused by atom number fluctuations (see text). The shaded area corresponds to the standard deviation of the distribution of n_0 induced by these initial fluctuations. The static bias is $q_0/h = 276$ Hz, the detuning $\delta/2\pi = -18$ Hz, and the modulation amplitude $\Delta q/h = 218$ Hz ($\kappa \simeq 0.36$). The interaction strength is $U_s/h \approx 32$ Hz for $t = 0$ and decays to ≈ 20 Hz for $t = 40$ s due to atom losses during the hold time in the optical trap. **b**: Long-time relaxation of the secular population $\overline{n}_0$ to a steady state. We attribute the small drift of the steady state population to the decay of U_s.

therefore to their dephasing after averaging over several realizations of the experiment. We believe that the main contribution comes from small ($\Delta N/N \sim 8\,\%$) fluctuations of the atom number. These fluctuations induce fluctuations $\Delta U_s/U_s \sim 6\,\%$ of the N−dependent interaction strength U_s [see Appendix B for the calibration of the dependence $U_s(N)$].

We show in Fig. 3 and Fig. 4 the theoretical results obtained by solving numerically Eqs.(8,9) with the dissipative term (16) for different interaction strengths U_s, and averaging over a Gaussian distribution of U_s with mean and variance deduced from the measured atom number statistics. We checked that for relatively short times (say, < 200 ms), the dissipation plays a negligible role and the observed damping of the oscillations is essentially due to the fluctuations of U_s.

In the remaining of this Section, we focus on the initial oscillations shown in Fig. 3, neglecting the role of dissipation, and postpone the discussion of relaxation at long times to Sec. IV.

B. Secular equations for near-resonant driving

For our experimental situation with $q_0 \gg U_s$ and for a modulation frequency close to the k_0 Shapiro resonance ($|\delta| \ll q_0$), we derive in Appendix D 1 effective equations of motion for the slowly evolving components by averaging over the fast micromotion. These secular equations of motion read

$$\hbar\dot{\overline{n}}_0 = 2\kappa U_s \overline{n}_0(1 - \overline{n}_0)\sin\phi, \tag{23}$$

$$\hbar\dot{\phi} = -\hbar\delta + 2U_s(1 - 2\overline{n}_0)(1 + \kappa\cos\phi). \tag{24}$$

Here, $\overline{n}_0$ is the time average of n_0 over one modulation period $T = 2\pi/\omega$, and the secular phase ϕ is related to the time-average $\overline{\theta}$ of the phase by

$$\phi = \overline{\theta} + k_0(\omega t + \varphi_{\text{mod}} + \pi/2). \tag{25}$$

The interaction terms driving the spin dynamics are renormalized by a factor

$$\kappa = J_{k_0}\left(\frac{2\Delta q}{\hbar\omega}\right), \tag{26}$$

with J_k the kth-order Bessel function of the first kind. Note that our modulation scheme is limited to $\Delta q < q_0$. Together with the secular approximation, this implies that $0 < \kappa < 1$.

The secular equations Eqs. (23,24) have a structure similar to the original spin-mixing equations Eqs. (8,9) with the replacements $q \rightarrow -\hbar\delta/2$ and $e^{i\theta} \rightarrow \kappa e^{i\phi}$. Accordingly, Eqs. (23,24) derive from the classical Hamiltonian of the secular motion with the canonical momentum $p_\phi = \hbar\overline{n}_0/2$,

$$\mathcal{H}_{\text{sec}}(p_\phi, \phi) = E_{\text{sec}}(\overline{n}_0 = 2p_\phi/\hbar, \phi) \tag{27}$$

and

$$E_{\text{sec}}(\overline{n}_0, \phi) = -\frac{\hbar\delta}{2}\overline{n}_0 + U_s\overline{n}_0(1 - \overline{n}_0)(1 + \kappa\cos\phi). \tag{28}$$

The different dynamical regimes are best understood in the limit of small driving, $\kappa \ll 1$. We show in Appendix D 2 that the secular equations Eqs. (23,24) reduce for $\kappa \rightarrow 0$ to the ones describing the motion of a one-dimensional rigid pendulum of natural frequency $\Omega = \sqrt{2\kappa}U_s/\hbar$, with the secular phase ϕ representing the angle of the pendulum. The pendulum admits two dynamical regimes, either oscillations around the stable equilibrium point $\phi = 0$, or full-swing rotations with ϕ running from 0 to 2π. The period of the oscillations diverges at the transition between the two regimes.

The same qualitative conclusions hold outside of the weak driving limit. A numerical solution of the equations of motion shows that the positions of the resonance and of the separatrix shift to slightly higher frequencies with increasing driving strength. From Eq. (25), we note that the regime of small oscillations ($\phi \approx 0$) corresponds to an atomic phase $\overline{\theta} \approx -k_0(\omega t + \varphi_{\text{mod}} + \pi/2)$ locked to the drive. Conversely, the regime of full-swing rotations ($\phi \approx -\delta t$) corresponds to a free-running atomic phase $\overline{\theta} \approx -2q_0 t/\hbar$, barely affected by the drive.

C. Measurement of the secular phase ϕ

In order to observe the two dynamical regimes, we now concentrate on the evolution of the phase ϕ, since the population $\overline{n}_0$ oscillates in both cases.

We measure the secular phase using a variant of the method of Section II B 2 that allows us to lift the phase

ambiguity. We measure $\cos\theta$ as before for stroboscopic times $t_p = pT$ and a quarter of period later $t_p + T/4$, with p a positive integer and $T = 2\pi/\omega$ the period of the modulation. Assuming $\phi(t_p) \approx \phi(t_p + T/4)$ (in accordance with the secular approximation), we obtain, after converting θ to ϕ using the definition of the latter in Eq. (25), a simultaneous measurement of $\sin\phi(t_p)$ and $\cos\phi(t_p)$ at stroboscopic times t_p.

Obtaining confidence intervals on the measurement of ϕ is far from obvious. The statistical spread of $\sin\phi(t_p)$ and $\cos\phi(t_p)$ can be quantified using the quantity $S = \langle\cos\phi\rangle^2 + \langle\sin\phi\rangle^2$, equal to 1 if ϕ is perfectly determined and vanishing for ϕ completely random. We find that S decreases with a characteristic time scale ~ 200 ms. Physically, we attribute this decay essentially to the fluctuations of U_s coming from atom number fluctuations translating into a phase spread increasing with time. Mathematically, the probability distribution $\mathcal{P}(\phi)$ of ϕ that derives from our expected distribution of U_s has a complicated shape due to the non-linearities of the spin-mixing equations. We did not pursue a sophisticated statistical analysis accounting for the peculiarities of $\mathcal{P}(\phi)$, and use instead the quantity S introduced above to estimate when the measurement of the phase is reliable. We arbitrarily choose the criterion $S \geq 1/2$ corresponding to measurements times $t \leq 200$ ms.

In an ideal experiment strictly described by Eq. (21), the modulation would be turned on instantaneously at $t = 0$. The initial phase $\theta(0) = 0$ would then be determined by the preparation of the initial state. In practice, a small delay of $\Delta t = 100\,\mu$s is present between the preparation and the beginning of the modulation, and the modulation settles to the form in Eq. (21) after $1 - 2$ ms, due to the transient response of the coils used to generate the modulation B_y. During this short transient ($\ll \hbar/U_\mathrm{s}$), the populations barely evolve but the phase changes because of the QZE. Both effects can be incorporated as an initial phase shift

$$\theta_0 = -\frac{2}{\hbar} \times \left[q_0 \Delta t + \int_0^{+\infty} [\tilde{q}(t) - q(t)]dt \right]. \quad (29)$$

Here $\tilde{q}$ denotes the instantaneous QZE actually experienced by the atoms and $q(t)$ the ideal step-like profile. The extra phase shift is $\theta_0 \approx -0.5$ rad for the data in Fig. 3**a1-2**. We can also insert on purpose a variable delay between the preparation step and the start of the modulation to tune the initial phase θ_0. We used this technique to record the data in Fig. 3**b1-2**, which are otherwise obtained for identical conditions as in Fig. 3**a1-2**.

We plot in Fig. 3 (right column) the results for ϕ for the first resonance $k_0 = 1$. For small detuning, the phase oscillates around $\phi = 0$, i.e. the dynamics of the BEC phase is phase-locked with the drive (panels **a1-2,b1-2.**). The excursion of the phase away from $\phi = 0$ depends on the detuning and the initial phase, which we can tune (panels **b1-2**) to have $\phi(t = 0) \simeq 0$. For a given initial phase, when δ exceeds a critical value corresponding to the transition betweeen the two dynamical regimes,
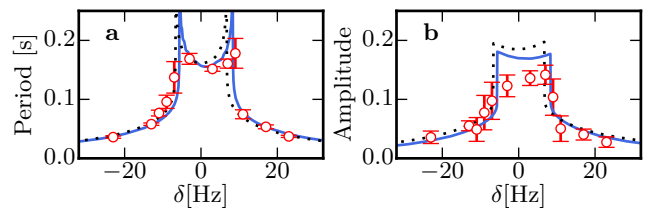

FIG. 5. Period (**a**) and amplitude (**b**) of the secular oscillations versus detuning δ for the same parameters as in Fig. 3. The solid blue lines show the numerical solutions of Eqs. (8,9), and the dotted black lines the analytical solution of the pendulum model.

phase locking no longer occurs and the BEC phase runs freely from 0 to 2π, corresponding to the "rotating pendulum" case (panels **c1-2**).

D. Period and amplitude of the secular oscillations

We extract the amplitude and period of the secular oscillations by fitting a periodic function $n_0(t) = \sum_{j=0}^3 a_j \cos(jt/T_\mathrm{sec} + \phi_0)$ to the data. We restrict the fit to the first two periods of the secular motion, with the amplitude $a_j \in \boldsymbol{R}$ of the harmonics and the initial phase ϕ_0 as free parameters. Fig. 5 shows the period T_sec and amplitude for the first resonance $k_0 = 1$ versus detuning. The results agree well with a numerical solution of Eqs. (8,9) (i.e., without taking dissipation into account), and with the pendulum model. Close to resonance, the measured amplitude is systematically lower than the theoretical prediction. This can be qualitatively explained by the presence of noncondensed atoms that do not participate in the coherent secular dynamics.

IV. LONG-TIME RELAXATION AND STEADY STATE

In this Section, we focus on the state reached for long evolution times, after relaxation has taken place. We observe that after the damping of the slow, large amplitude Shapiro oscillations, the population $\bar{n}_0$ reaches a steady state that persists for tens of seconds [59]. We characterize this steady state and show that it can differ from the equilibrium points of either the non-driven Hamiltonian $\mathcal{H}$ or the secular Hamiltonian $\mathcal{H}_\mathrm{sec}$. We then take explicitly into account the dissipation using the two models DM 1 and DM 2 introduced in Sec. II C 2. We show that DM 2 leads to predictions in good agreement with our observations, whereas DM 1 is clearly excluded. Then, we study the new fixed points that can appear in the presence of this dissipation, and we discuss their stability. In particular there exist some regions of parameter space where two fixed points can be simultaneously stable or metastable. This leads to the possibility of observing a hysteretic behavior, which we confirm experimentally.
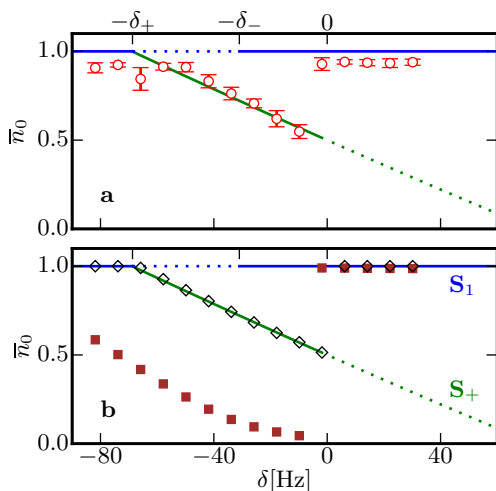
FIG. 6. **a**: Measured population n_0 as a function of detuning δ after a relaxation time of 10 s. The experiment is performed near the first resonance $k_0 = 1$ ($\hbar\omega \approx 2q_0$) with $n_{0,\mathrm{i}} = 0.5$. The static bias is $q_0/h \approx 277$ Hz, the modulation amplitude is $\Delta q/h \approx 227$ Hz ($\kappa \simeq 0.4$), and the interaction strength is $U_\mathrm{s}/h \approx 26$ Hz. **b**: Numerical solutions of the dissipative models 1 (Eq. 15, brown squares) and 2 (Eq. 16, black empty diamonds). In both panels, the horizontal blue (respectively oblique green) line corresponds to the stationary state S_1 (resp. S_+). The solid (resp. dotted) segments correspond to the stable (resp. unstable) region according to DM 2 (see Section IV B).

A. Observation of a Non-Equilibrium Steady State

Fig. 6 shows a typical measurement for strong driving ($\kappa = 0.38$) near the first resonance $k_0 = 1$. We monitor how the steady state value changes as a function of detuning δ. We find that the system relaxes to $\overline{n}_0 \approx 1$, except in a range of negative detunings close to the resonance where the population $\overline{n}_0$ takes values between ≈ 0.5 and 1. The steady state reached in this strongly driven situation does not correspond to the thermodynamic equilibrium point in the absence of modulation, *i.e.* the ground state of $\mathcal{H}$ defined in Eq. (11) with $q(t) = q_0$, obtained for $\overline{n}_0 = 1$. It does not correspond either to the minimum of the secular Hamiltonian $\mathcal{H}_\mathrm{sec}$ defined in Eq. (27), obtained for $\overline{n}_0 = 1$ for $\delta > 0$ and $\overline{n}_0 = 0$ for $\delta < 0$. This contrasts strongly with the non-driven case where the thermodynamic equilibrium state $n_0 \approx 1$ is always observed at long times.

In the experimental results shown in Fig. 1**c**, we observe the same behaviour for higher resonances, up to $k_0 = 8$ (limited by the maximal magnetic field we can produce). In order to record this set of data, we set $\omega/2\pi = 100$ Hz and scanned simultaneously the bias value q_0 and driving strength Δq, keeping $\Delta q/q_0$ and therefore the secular renormalization factor κ approximately constant. After a wait time of 30 s, we observed that the system relaxes for all k_0 to the same station-
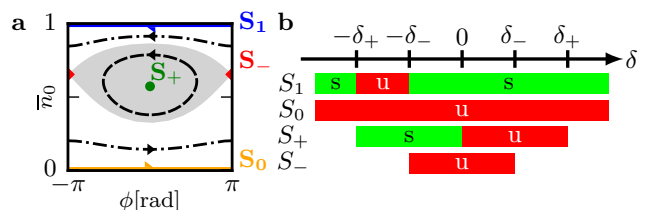

FIG. 7. Fixed points of the dissipative spin-mixing model 2. **a**: Phase space portrait of the stationary solutions of Eqs. (23,24). The two limit cycles are labeled S_0 ($\overline{n}_0 = 0$, solid orange line) and S_1 ($\overline{n}_0 = 1$, solid blue line) and the two fixed points S_+ (green dot) and S_- (red diamond). The black lines show typical trajectories in the oscillating (dashed line) or rotating (dash-dotted lines) regimes. The shaded area covers the oscillating regime. The plot is shown for $\delta/2\pi = -10$ Hz, $U_\mathrm{s}/h = 25$ Hz, $\kappa \simeq 0.38$ ($\delta_-/2\pi \simeq 32$ Hz) and a damping coefficient $\beta_2 \to 0^+$. **b**: Table summarizing for $\beta_2 \to 0^+$ the ranges of detuning where each stationary solution is stable ('s') or unstable ('u'). The boundaries $\delta_\pm$ are defined after Eq. (31).

ary state as for the first resonance. In the following, we therefore concentrate on the case $k_0 = 1$ as in the previous Section.

We use the same dissipative models introduced in Section II C 2 to explain the experimental observations. We show in Fig. 6**b** the result of a direct numerical solution (with no secular approximation) of Eqs. (13,14) for the dissipative models 1 and 2. We observe that the DM 1 fails to reproduce the measured steady state populations, while the DM 2 predicts a long-time behaviour consistent with the experimental results. This contrasts with the non-driven case, where both models lead to similar predictions. In the following, we specialize to the DM 2 and explore its consequences for the long-time steady state.

B. The fixed points and their stability

We now look for (possibly metastable) secular solutions of dissipative model 2 where the population $\overline{n}_0$ is stationary. We derive generalized secular equations as in Section III starting from Eqs (13,14,16) defining the DM 2. Observing from Eq. (25) that $\dot{\overline{\theta}} \approx -\omega + \dot{\phi}$, we find

$$\hbar\dot{\overline{n}}_0 = \overline{n}_0(1 - \overline{n}_0)\left(2\kappa U_\mathrm{s}\sin\phi + \beta_2\hbar\omega - \beta_2\hbar\dot{\phi}\right). \quad (30)$$

The phase dynamics is still determined by Eq. (24). From Eq. (30), we identify four possible states for which $\dot{\overline{n}}_0 = 0$.

The first two states correspond to $\overline{n}_0 = 0, 1$. In these two limiting cases, the relative phase θ (and thus ϕ) is physically irrelevant and can take any value. These two solutions, labeled S_0, S_1 in the following, correspond to "limit cycles" in the language of dynamical systems [60]. The other two stationary states, labeled $S_\pm$, correspond to fixed points of the dissipative equations of motion where $\dot{\overline{n}}_0 = \dot{\phi} = 0$. They correspond to the secular

phases $\phi_+ = \epsilon, \phi_- = \pi - \epsilon$, where the angle ϵ obeys $\sin \epsilon = -\beta_2 \hbar \omega / (2\kappa U_s)$. The populations at the fixed points are

$$\overline{n}_{0,\pm} = \frac{1}{2}\left(1 - \frac{\delta}{\delta_\pm}\right), \tag{31}$$

with:

$$\hbar \delta_\pm = 2U_s(1 \pm \kappa \cos \epsilon). \tag{32}$$

Fig. 7a shows the location of the stationary solutions in a secular phase-space portrait $(\overline{n}_0, \phi)$. For each sign of the detuning δ, one of the two limit cycles $S_{0,1}$ corresponds to the minimum of the secular energy E_{sec}. The fixed point S_+ is always the maximum of E_{sec} and S_- is a saddle point.

Dissipation must be present, but not too strong, in order to ensure the existence of an attractive fixed point of the dynamics. Indeed, the fixed points $S_\pm$ disappear when $\beta_2 \geq 2\kappa U_s / (\hbar \omega)$. If the dissipation stength β_2 is too large or the driving strength too small, the drive cannot provide enough energy to overcome the dissipation and create a metastable state. This is confirmed by other experiments that we performed with a weaker driving strength $\kappa \sim 0.08$, where we found that the relaxation to the fixed point was less robust than the one shown in Fig. 6.

For the experiments shown in Fig. 6, we find $\phi_+ \approx 0.04$ corresponding to the weak dissipation limit, $\epsilon \propto \beta_2 \to 0^+$. In this situation, the positions of the fixed points are well approximated by $\hbar \delta_\pm \approx 2U_s(1 \pm \kappa)$. They are therefore independent of the precise value of β_2 to first order in the small parameter ϵ.

We study the dynamical stability of the stationary solutions in App. F for a phenomenological damping coefficient $\beta_2 \to 0^+$. We summarize the results in Fig. 7b. The drive destabilizes S_1 in a small region of positive detunings around the resonance, while S_0 is always unstable because of the dissipation. The fixed point S_+ is stable only for $\delta < 0$, while S_- is always unstable.

At first glance, one may expect that energy dissipation always induces relaxation to an energy minimum. In fact, at the fixed point $S_\pm$, the atomic phase locks to the drive with a small phase lag, such that the power absorbed from the drive exactly compensates the power loss due to dissipation. This phase-locking enabled by dissipation stabilizes the system in a highly excited state (App. D 3), reminiscent of the dissipative phenomenon leading to Shapiro steps in SCJJs [4].

C. Interpretation of experimental results

We can now interpret the experimental findings of Fig. 6. The position of the stable fixed point S_+ in the limit $\beta_2 \to 0$ is shown in Fig. 6, and explains well the observed steady state populations for $\delta \in [-\delta_+, 0]$. Outside this window, the system relaxes to the equilibrium
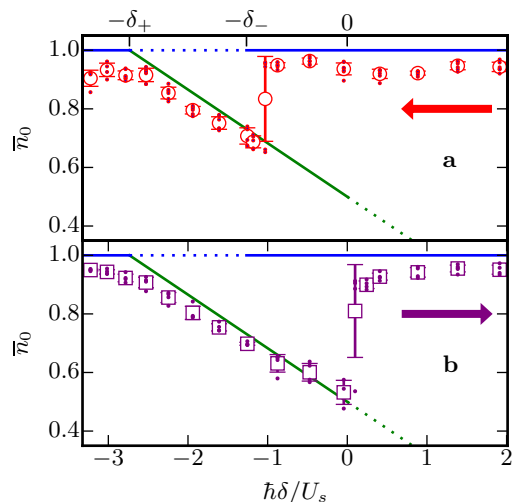

FIG. 8. Observation of hysteresis in the relative population n_0 after a detuning ramp. We prepare a spinor BEC with $n_{0,\mathrm{i}} \simeq 1$, and scan the detuning by changing q_0 for fixed $\omega/2\pi = 277\,\mathrm{Hz}$ and $\Delta q/h = 227\,\mathrm{Hz}$. In **a** (respectively, **b**), the ramp decreases (resp., increases) from $\delta_i \approx 2.0\,U_s/\hbar$ (resp., $\delta_i \approx -3.3\,U_s/\hbar$). The horizontal blue (resp., oblique green) line correspond to S_1 (resp., S_+). The solid (resp., dotted) segments corresponds to the stability (resp., instability) regions. The small dots show individual measurements, the squares their average, and the error bars their standard deviation.

state S_1 with $n_0 \approx 1$. We interpret the observed "trapping" in the state S_+ as follows. A system prepared with $n_{0,\mathrm{i}} \approx 0.5$ tends to relax to the ground state S_1 of $\mathcal{H}$, as observed for $|\delta| > \delta_+$ where there is no fixed point. For $\delta \in [-\delta_+, 0]$, the derivative of the phase $\dot{\phi}$ diminishes in absolute value as $\overline{n}_0$ increases because of the dissipation, and it progressively vanishes. At this point, which corresponds to S_+, $\dot{\overline{n}}_0$ also vanishes and the system remains trapped in this state. On the contrary, for $\delta \in [0, \delta_+]$, S_+ corresponds to $\overline{n}_{0,+} \leq 1/2$ and $|\dot{\phi}|$ increases as $\overline{n}_0$ increases. The trajectory tends to move the system away from S_+. As a result, dissipation acts as in the non-driven case and the system eventually reaches S_1.

The scenario described above explains all observations but one. In Fig. 1c, for very small but negative δ near the first resonance, the system relaxes to $\overline{n}_0 \simeq 0.16$. This observation is consistent with thermalization in the secular Hamiltonian where the lowest energy state is $\overline{n}_0 = 0$ when $\delta < 0$. The residual deviation with respect to $\overline{n}_0 = 0$ observed experimentally may be due to a non-zero thermal fraction or an incomplete thermalization.

D. Hysteretic Behavior

According to the stability diagram of Fig. 7b, there is no single stationary solution that would be stable for all detunings δ. Furthermore, there are two stable solu-

tions S_+ and S_1 in the interval $[-\delta_-, 0]$. In such a situation, one can expect some hysteretic behaviour, which we searched for using a slightly different procedure than in the rest of the article.

We prepared a BEC in the state $m = 0$, such that $\overline{n}_{0,i} \sim 1$ (up to thermal atoms in $m = \pm 1$). We apply the modulation as before but slowly ramp the static bias q_0 over a ramp time of $3\,\mathrm{s}$, and then hold the driven system at the final q_0 value for $7\,\mathrm{s}$. This amounts to a slow ramp of the detuning δ decreasing (respectively, increasing) from δ_i to δ_f in Fig. 8**a** (resp., Fig. 8**b**). For decreasing ramps with $\delta_i > \delta_+$, the system remains in S_1 in the domain $\delta > -\delta_-$ where S_1 is stable. Continuing the ramp further, S_1 becomes unstable and we find that the system relaxes to S_+ as in the previous experiments. Conversely, for an increasing ramp starting from $\delta_i < -\delta_+$, the system follows S_+ while it is stable, *i.e.* for $\delta_f \in [-\delta_+, 0]$ and S_1 otherwise. We therefore observe an hysteresis cycle spanning the interval $\delta \in [-\delta_-, 0]$ where both S_1 and S_+ are stable.

V. CONCLUSION

In conclusion, we have observed the analogue for a driven spin-1 BEC of the Shapiro resonances characteristic of the AC Josephson effect in SCJJs. The population dynamics near each resonance corresponds to a slow and non-linear secular oscillation on top of a rapid micromotion. We have found that the driven spin-1 BEC relaxes at long times to asymptotic states phase-locked to the drive and that are not stable without it. We proposed a phenomenological model of dissipation that describes quantitatively the relaxation process and its outcome. The dynamics in the driven case allows us to discriminate between different phenomenological models, in contrast to the situation without driving where these different models lead to similar predictions.

The microscopic origin of the dissipation remains to be investigated. While dissipation probably comes from interactions between condensed and noncondensed atoms, a quantitative description of these interactions and of the resulting thermalization process is lacking. The procedure we used in this paper led to a set of dissipative equations which are essentially generalized Gross-Pitaevskii equations. While we have found excellent agreement between the experimental results and the predictions of these equations, our procedure is purely phenomenological and whether these generalized Gross-Pitaevskii equations can be derived from first principles or not remains an open question. A detailed microscopic study of dissipation in this setup would also be useful to understand other types of driven quantum gases where an optical lattice potential [61] or the interaction strength [62] are modulated.

Another interesting question is related to the occurence of deterministic chaos in a spinor BEC [63]. Without driving, chaotic behavior can be ruled out for a spin-1 BEC on the basis of the Poincaré-Bendixson theorem [60]: the dynamics is indeed obtained from the one-dimensional Hamiltonian $\mathcal{H}$, with only two variables θ and $p_\theta \sim n_0$. To allow for a chaotic behavior, one needs to consider higher spin BECs [64] or driven spin-1 BECs [63], with time playing the role of a third variable. However when the secular approximation holds, we recover an effective time-independent one-dimensional problem with the Hamiltonian $\mathcal{H}_{\mathrm{sec}}(p_\phi \sim n_0, \phi)$, which excludes again a chaotic behavior. One thus expects to find chaos only in situations where the secular approximation breaks down. Using the non-dissipative spin-mixing equations and adapting the methods of [63] to our system, we have found numerically that chaos can be present in the vicinity of Shapiro resonances for strong modulation and small bias, $\Delta q \sim q_0 \sim U_{\mathrm{s}}$. For almost all experiments reported in this paper, where $q_0 \gg U_{\mathrm{s}}$, we did not find any evidence of chaotic behaviour. The only exception is the situation investigated in Fig. 1**c**., where $q_0 \simeq h \times 100$ Hz is only three times larger than U_{s}. The deviation from the fixed point near $\delta = 0$ for the first resonance could be connected to the onset of chaotic behavior, which is an interesting direction to explore in future work.

Finally, a promising application of driven spinor gases is the dynamical control of the strength of spin-mixing interactions, viewed as a matter-wave equivalent of parametric amplifiers in quantum optics. Such parametric amplifiers are phase-sensitive, and are also known to generate squeezing (see [30, 32, 65] for the spinor case). This enables interferometric measurements below the standard quantum limit [29, 31, 66, 67]. A promising direction for the development of devices operating at the Heisenberg-limit are the so-called $SU(1,1)$ interferometers [31, 67], which can be viewed as Mach-Zehnder interferometers where the beam splitters are replaced by parametric amplifiers. As shown in Appendix E, the quantum version of the secular single-mode Hamiltonian [20] is renormalized by driving as in the mean-field Gross–Pitaevski framework. This implies that spin-mixing collisions can be enabled by moving close to a Shapiro resonance for a controllable duration, and then disabled by detuning the system away from resonance. Such dynamical control over the spin-mixing process could significantly improve the performances of matter-wave $SU(1,1)$ interferometers [31].
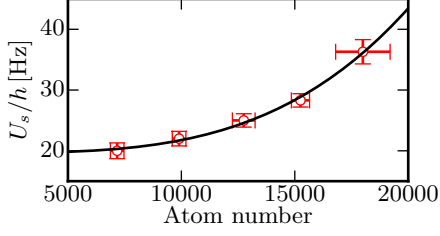
FIG. 9. Interaction strength U_s measured for different atom number. The black solid line is an heuristic fit (see main text). The QZE is static and equal to $q_0/h \approx 0.7\,\text{Hz} \ll U_s$ ($B_x \approx 50\,\text{mG}$).

Appendix A: Adiabatic following

We consider a gas of spin-1 atoms in a magnetic field $\boldsymbol{B} = B(t)\boldsymbol{u}(t)$ with time-dependent amplitude B and orientation $\boldsymbol{u}$. We take the instantaneous direction $\boldsymbol{u}(t)$ of $\boldsymbol{B}$ as quantization axis. The label $m = 0, \pm 1$ then corresponds to the instantaneous Zeeman state $|m\rangle_{\boldsymbol{u}}$, i.e. the eigenstate of $\boldsymbol{\hat{f}} \cdot \boldsymbol{u}$ with eigenvalue m, with $\hat{f}_{x,y,z}$ the spin-1 matrices. The atomic spins precess around $\boldsymbol{u}$ at the characteristic Larmor frequency $\omega_L = \mu_B B/2$. The atom internal state follows adiabatically changes of B and $\boldsymbol{u}$ if the adiabatic condition $\dot{\omega}_L \ll \omega_L^2$ holds at all times. Here the dot denotes a time derivative. In our experiment, this condition can also be written $\omega B_y \ll \omega_L |\boldsymbol{B}|$. In most of this work, the Larmor frequency is around $\omega_L \sim 2\pi \times 0.7\,\text{MHz}$. Since $B_y \leq |\boldsymbol{B}|$, the sufficient condition $\omega/\omega_L \sim 10^{-3} \ll 1$ is always fulfilled.

Appendix B: Calibration of U_s

We calibrate the interaction strength U_s using the well-established behavior of spin-mixing oscillations without driving [21–25]. For a given total atom number N, we fit the observed population oscillations with the numerical solutions of Eqs. (8,9) treating U_s as a free parameter, all other parameters being kept constant. We show the fitted values of U_s versus N in Fig. 9. The dependence on atom number reflects the fact that our experiments are in the crossover between the ideal gas (where U_s is independent of N) and the Thomas-Fermi regime (where $U_s \propto N^{2/5}$). We use the heuristic function $U_s(N)/h = a(1 + (N/N_0)^b)$ to calibrate the dependence, with best fit parameters $a \simeq 20\,\text{Hz}$, $b \simeq 3.5$ and $N_0 \simeq 19\,000$. Small fluctuations of N induce fluctuations of U_s according to $\delta U_s = ab(N/N_0)^b \delta N/\langle N \rangle$. In our experiment, we have typically $\langle N \rangle \simeq 13\,000$ and $\delta N \simeq 1\,000$, which correspond to $\langle U_s \rangle/\hbar \simeq 25\,\text{Hz}$ and $\delta U_s/\hbar \simeq 1.5\,\text{Hz}$.

Appendix C: Relaxation of spin oscillations without driving

The spin dynamics without driving consists of a "fast" evolution of the population and of the relative phase θ superimposed on a slowly-varying envelope $\overline{\overline{n}}_0$. In the limit $q_0 \gg U_s$, the envelope of n_0 relaxes to $n_0 = 1$ over times long compared to the period $\sim \hbar/(2q_0)$ of spin-mixing oscillations. Averaging in a time window long compared to this period, we obtain effective equations for $\overline{\overline{n}}_0$ that can be solved analytically. For the dissipative model 1 with the initial condition $n_0(0) = n_{0,\text{i}}$, we find that $\overline{\overline{n}}_0$ obeys the implicit equation, $f(\overline{\overline{n}}_0) = f(n_{0,\text{i}}) + t/\tau_1$, with $f(x) = 2\ln[x/(1-x)] + (2x-1)/[x(x-1)]$ and $\tau_1 = \hbar q_0/(\beta_1 U_s^2)$. For $t \gg \tau_1$, the solution is well approximated by Eq. (18). For the dissipative model 2, we obtain Eq. (19) by direct integration.

Appendix D: Secular dynamics

1. Derivation of the secular equations

In this Section, we derive the secular equations Eqs. (23,24). Integrating formally Eq. (9), we rewrite $\theta = \alpha - 2p$, where

$$p(t) = \frac{1}{\hbar} \int_0^t q(t')dt' = \overline{p} - \frac{\eta}{2}\cos(\omega t + \varphi_{\text{mod}}). \quad \text{(D1)}$$

Here $\overline{p} = \frac{q_0 t}{\hbar} + \frac{\chi}{2}$ and α verifies $\hbar\dot{\alpha} = 2U_s(1 - 2n_0)(1 + \cos\theta)$. We introduced a modulation index $\eta = 2\Delta q/(\hbar\omega)$ and an initial phase $\chi = \eta\cos\varphi_{\text{mod}}$.

We now assume that the driving frequency is close to a parametric resonance, i.e. $\omega \sim 2q_0/(\hbar k_0)$ for some integer k_0, and that $q_0 \gg U_s$. All physical variables feature in general a large-amplitude secular motion occurring on time scales much longer than the modulation period, plus rapidly-varying terms oscillating at harmonics of $2q_0/\hbar$ that describe the micromotion. In the regime $q_0 \gg U_s$, the amplitude $\sim U_s/q_0$ of the micromotion of n_0 and α is small. Taking the time average over one period of the modulation, $\overline{\cdot} = \frac{1}{T}\int_0^T dt\cdot$, eliminates the micromotion in Eqs. (8,9),

$$\hbar\dot{\overline{n_0}} \approx 2U_s\overline{n_0}(1 - \overline{n_0})\overline{\sin\theta}, \quad \text{(D2)}$$

$$\hbar\dot{\overline{\alpha}} \approx 2U_s(1 - 2\overline{n_0})\left(1 + \overline{\cos\theta}\right). \quad \text{(D3)}$$

We compute the time average of trigonometric functions of θ using the Jacobi-Anger expansion, $e^{ia\sin(\theta)} = \sum_{k=-\infty}^{+\infty} J_k(a)e^{ik\theta}$, with J_k a Bessel function of the first kind. Neglecting the micromotion of α, we can write $\overline{e^{i\theta}} \approx e^{i\overline{\alpha}}\overline{e^{-2ip}}$, with

$$e^{-2ip} = \sum_{k=-\infty}^{+\infty} J_k(\eta)e^{i\left(-\frac{2q_0}{\hbar} + k\omega\right)t + ik(\phi_{\text{mod}} + \pi/2) - i\chi}. \quad \text{(D4)}$$

The term $k = k_0$ in the expansion gives rise to a slowly varying secular contribution, while all other terms average out over one period of the modulation. Neglecting the non-resonant terms, we obtain $\overline{e^{-2ip}} = \kappa e^{i\zeta(t)}$, with $\hbar\delta = 2q_0 - k_0\hbar\omega$, $\zeta(t) = k_0(\phi_{\rm mod} + \pi/2) - \chi - \delta t$ and $\kappa = J_{k_0}(\eta)$. This finally leads to

$$\overline{e^{i\theta}} \approx \kappa e^{i\phi} \tag{D5}$$

where the secular phase $\phi = \zeta + \overline{\alpha}$ is defined as

$$\phi = -\delta t + \overline{\alpha} + k_0(\varphi_{\rm mod} + \pi/2) - \chi. \tag{D6}$$

Eqs. (23,24) follow from Eqs. (D2,D3,D5,D6).

From Eq. (D6), we can relate ϕ to the atomic phase, $\overline{\theta} = \phi - k_0(\omega t + \varphi_{\rm mod} + \pi/2)$. This equality shows that when ϕ is oscillating, θ also oscillates around the phase of the drive $-k_0(\omega t + \varphi_{\rm mod} + \pi/2)$, up to a constant.

2. Rigid Pendulum Model

In the weak driving regime, $\kappa \ll 1$, the $\kappa \cos\phi$ term in Eq. (24) is negligible. Moreover, the amplitude of variation of $\overline{n}_0$ is small. To prove the last point, we integrate Eqs. (23,24) and obtain the implicit equation $\left[g(x)\right]_{\overline{n}_{0,i}}^{\overline{n}_0(t)} = -\kappa\left[\cos x\right]_{\phi_i}^{\phi(t)}$, with $g(x) = \left(1 - \frac{\hbar\delta}{2U_{\rm s}}\right)\ln\left(\frac{x}{1-x}\right) + 2\ln(1-x)$. This implies that the amplitude of variation of $\overline{n}_0$ is indeed small when $\kappa \ll 1$. This allows us to linearize Eq. (23).
With the initial condition $n_{0,i} = 1/2$, we obtain $\hbar\dot{\overline{n}}_0 \simeq \frac{\kappa U_{\rm s}}{2}\sin\phi$. Taking the time derivative of Eq. (24), we then find that the phase obeys the pendulum equation

$$\ddot{\phi} + \Omega^2 \sin\phi = 0, \tag{D7}$$

with natural frequency $\Omega = \sqrt{2\kappa U_{\rm s}}/\hbar$. The angular velocity of the pendulum $\dot{\phi}$ is determined by $\dot{\phi} = -\delta + 2U_{\rm s}(1 - 2\overline{n}_0)$.

3. Energy balance

In this Section, we compute the power delivered by the drive in the framework of DM 2. In particular, we show that at the fixed points $S_\pm$, it compensates for the dissipated energy. For simplicity, we focus on the first resonance $k_0 = 1$ and assume $\kappa \ll 1$.
The time derivative of the total energy is

$$\frac{dE_{\rm spin}}{dt} = \mathcal{P}_{\rm drive} + \mathcal{P}_{\rm diss}^{(2)}, \tag{D8}$$

with $\mathcal{P}_{\rm drive} = -\dot{q}n_0$, and $\mathcal{P}_{\rm diss}^{(2)} = -\frac{\hbar}{2}\beta_2 n_0(1 - n_0)\dot{\theta}^2$. We introduce $\tilde{n}_0$, the component of n_0 oscillating at $\sim \omega$. The product $\dot{q}\tilde{n}_0$ does not vanish after taking the time-average in the expression for $\mathcal{P}_{\rm drive}$.

From Eq. (D4), the $k = 0$ component of $\sin\theta$ oscillating at $\sim \omega$ is $\widetilde{\sin\theta} = -\cos(\omega t + \varphi_{\rm mod} - \phi)$. The amplitude of

the sidebands near-resonant with the drive [term $k = 2$ in Eq. (D4)] are negligible in the limit $\kappa \ll 1$. Using $\tilde{n}_0 = \mathcal{O}(U_{\rm s}/q_0) \ll 1$ to simplify Eq. (8), we find

$$\tilde{n}_0 = -\frac{2U_{\rm s}}{\hbar\omega}\overline{n}_0(1 - \overline{n}_0)\sin(\omega t + \varphi_{\rm mod} - \phi). \tag{D9}$$

Using $\kappa \simeq \Delta q/(\hbar\omega)$ (true if $\kappa \ll 1$), the average power delivered by the drive is finally

$$\overline{\mathcal{P}}_{\rm drive} = -\omega\kappa U_{\rm s}\overline{n}_0(1 - \overline{n}_0)\sin\phi. \tag{D10}$$

When there is no dissipation, this expression can be written as $\overline{\mathcal{P}}_{\rm drive} = -\hbar\omega\dot{\overline{n}}_0/2$. This result has a microscopic interpretation if one treats the driving field as a quantized electromagnetic field. One photon is absorbed to promote a pair of atoms in the $m = 0$ state to a pair with one atom in $m = +1$ and another in $m = -1$. The energy in the field is, up to a constant, $E_{\rm field} = N\hbar\omega n_0/2$, and $\overline{\mathcal{P}}_{\rm drive}$ correspond to the energy per unit time transferred back and forth from the field to the atoms. Eq. (D8) can also be interpreted as a statement that $N\overline{E}_{\rm spin} + \overline{E}_{\rm field}$ is constant.

With dissipation, the system relaxes to the fixed point S_+ or to S_0. The second case is trivial, since the drive and dissipated power both vanish. Let us discuss the first case. At the fixed points S_+, the atomic phase is locked to the drive, i.e. $\dot{\theta} \approx -\omega$ and $\overline{\mathcal{P}}_{\rm diss}^{(2)} \approx -\frac{\hbar\omega^2}{2}\beta_2\overline{n}_0(1 - \overline{n}_0)$. The energy balance can be rewritten as

$$\left.\frac{dE_{\rm spin}}{dt}\right|_{S_+} \approx -\omega\overline{n}_0(1 - \overline{n}_0)\left[\kappa U_{\rm s}\sin\phi_+ + \frac{\beta_2\hbar\omega}{2}\right], \tag{D11}$$

The term in brackets in the right hand side of Eq. (D11) vanishes exactly, as the secular phase takes the value $\sin\phi_+ = -\beta_2\hbar\omega/(2\kappa U_{\rm s})$ at S_+ (see Sec. IV B). At the fixed point, the phase lag between the atomic phase and the drive is therefore such that the power delivered by the drive exactly compensates for the energy dissipation.

Appendix E: Quantum treatment of the modulated SMA Hamiltonian

We start from the SMA Hamiltonian in Eq. (2), which we rewrite as

$$\hat{H}_{\rm spin} = -q(t)\hat{N}_0 + \frac{U_{\rm s}}{2N}\left(\hat{V} + \hat{W} + \hat{W}^\dagger\right).$$

We defined the operators $\hat{V} = \hat{S}_z^2 + 2\hat{N}_0(N - \hat{N}_0)$ and $\hat{W} = 2(\hat{a}_0^\dagger)^2\hat{a}_{+1}\hat{a}_{-1}$. Applying the unitary transformation

$$\hat{U}_1 = e^{-i\int_0^t \frac{q(t')dt'}{\hbar}\hat{N}_0} = e^{-ip\hat{N}_0}, \tag{E1}$$

the transformed Hamiltonian $\hat{H}' = \hat{U}_1\hat{H}\hat{U}_1^\dagger + i\hbar\frac{d\hat{U}_1}{dt}\hat{U}_1^\dagger$ reads

$$\hat{H}_1 = \frac{U_{\rm s}}{2N}\left[\hat{V} + \hat{U}_1\left(\hat{W} + \hat{W}^\dagger\right)\hat{U}_1^\dagger\right]. \tag{E2}$$

We introduce the Fock basis $|N_0, M_z\rangle$ with $N_{\pm 1} = (N - N_0 \pm M_z)/2$. The operators $\hat{W}$ (respectively $\hat{W}^\dagger$) only couples states with $M_z = M_z'$ and $N_0 = N_0' + 2$ (resp. $N_0 = N_0' - 2$). As a result, the matrix elements of $\hat{U}_1 \hat{W} \hat{U}_1^\dagger$ in the Fock basis are the same as the ones of $e^{-2ip}\hat{W}$, implying the equality of both operators.

We now derive an effective Hamiltonian describing the slow secular dynamics. We proceed as in Section D 1, using the Jacobi-Anger expansion to rewrite the phase factors and taking the time average over one period of the modulation assuming small detuning δ. We obtain an effective time-averaged Hamiltonian,

$$\overline{\hat{H}_1} = \frac{U_s}{2N}\hat{V} + \frac{\kappa U_s}{2N}\left(e^{i\zeta(t)}\hat{W} + e^{-i\zeta(t)}\hat{W}^\dagger\right). \qquad \text{(E3)}$$

We finish the calculation with a second unitary transformation $\hat{U}_2 = e^{-i\frac{\zeta(t)}{2}\hat{N}_0}$ to obtain an effective time-independent Hamiltonian

$$\hat{H}_{\text{eff}} = -\frac{\hbar\delta}{2}\hat{N}_0 + \frac{U_s}{2N}\hat{V} + \frac{\kappa U_s}{2N}\left(\hat{W} + \hat{W}^\dagger\right). \qquad \text{(E4)}$$

With a mean-field *ansatz* for the many-body spin state, we obtain from this effective Hamiltonian the same secular energy E_{sec} [Eq. (28)] as in the classical treatment, *i.e.* mean-field approximation and time averaging can be done in any order.

Appendix F: Stability of the stationary solutions of dissipative model 2.

1. Stability of the fixed points $S_\pm$

To discuss the stability of the fixed points $S_\pm$, we linearise Eqs. (30,24) using $\overline{n_0} = \overline{n}_{0,\pm} + \delta\overline{n}_{0,\pm}$ and $\phi = \phi_\pm + \delta\phi_\pm$. We find

$$\hbar\begin{pmatrix} \dot{\delta\overline{n}}_{0,\pm} \\ \dot{\delta\phi}_\pm \end{pmatrix} = M_\pm \begin{pmatrix} \delta\overline{n}_{0,\pm} \\ \delta\phi_\pm \end{pmatrix}, \qquad \text{(F1)}$$

$$M_\pm = \begin{pmatrix} 0 & \pm 2\kappa U_s n_{0,\pm}(1 - n_{0,\pm})\cos\epsilon \\ -2\hbar\delta_\pm & -2\kappa U_s\frac{\delta}{\delta_\pm}\sin\epsilon \end{pmatrix}.$$

The solutions are stable if the eigenvalues of the matrices $M_\pm$ have negative real parts. For simplicity, we consider the situation $|\sin\epsilon| = \beta_2\hbar\omega/(2\kappa U_s) \ll 1$. One can show

that the results below hold as long as $\beta_2\hbar\omega/(2\kappa U_s) < 1$, the same condition as for the existence of the fixed points.

In the limit $\epsilon \ll 1$, the eigenvalues of M_+ are approximately given by $X_{+,1} \simeq \beta_2\hbar\omega\frac{\delta}{2\delta_+} + i\sqrt{\Delta}$, and $X_{+,2} = X_{+,1}^*$, with $\Delta = 8\overline{n}_{0,+}(1 - \overline{n}_{0,+})\kappa(1 + \kappa)U_s^2$. Therefore, S_+ is stable for $\delta < 0$, and unstable otherwise. Turning to S_-, the eigenvalues are $X_{-,1} \simeq \sqrt{\Delta}$ and $X_{-,2} \simeq -X_{-,1}$ to leading order in β_2, and S_- is therefore always unstable. Note that our conclusions are established for the experimentally relevant case $0 \le \kappa < 1$. The roles of $S_\pm$ would be reversed for $\kappa < 0$.

2. Stability of the limit cycles $S_{0,1}$

We focus first on S_1. We consider small deviations, *i.e.* $\overline{n}_0 = 1 - \epsilon$ and linearize Eqs. (30,24) to the lowest order in ϵ,

$$-\hbar\dot{\epsilon} = 2\kappa U_s \sin\phi\epsilon + 2\beta_2 q_0\epsilon, \qquad \text{(F2)}$$

$$\hbar\dot{\phi} = -\hbar\delta - 2U_s(1 + \kappa\cos\phi). \qquad \text{(F3)}$$

We integrate Eq. (F2),

$$\Big[\ln\epsilon\Big]_{\epsilon(0)}^{\epsilon(t)} = -\frac{2\kappa U_s}{\hbar}\int_0^t \sin\phi(t')dt' - \frac{2\beta_2 q_0 t}{\hbar}.$$

Making the change of variable $t \to \phi$ and using Eq. (F3), we find

$$\epsilon(t) = \epsilon(0)e^{-4t/\tau_2}\frac{1 + a_1\cos\phi(0)}{1 + a_1\cos\phi(t)}, \qquad \text{(F4)}$$

$$\hbar\dot{\phi} = -(2U_s + \hbar\delta)(1 + a_1\cos\phi(t)). \qquad \text{(F5)}$$

with $a_1 = 2\kappa U_s/[2U_s + \hbar\delta]$ and $\tau_2 = 2\hbar/(\beta_2 q_0)$. If $|a_1| < 1$, ϵ is bound to a vincinity of $\epsilon(0)$. If $|a_1| > 1$, eq. (F5) shows that ϕ must vanish, which results in a divergency of ϵ. Therefore, $\epsilon(t)$ diverges iif $|a_1| > 1$. This defines the instability region of S_1 as $\delta \in [-2U_s(1+\kappa), -2U_s(1-\kappa)]$. This result is independent of the precise value of β_2 as long as it is strictly positive. A similar calculation for S_0 with $\epsilon = \overline{n}_0$ yields

$$\epsilon(t) = \epsilon(0)e^{4t/\tau_2}\frac{1 + a_0\cos\phi(0)}{1 + a_0\cos\phi(t)}, \qquad \text{(F6)}$$

with $a_0 = 2\kappa U_s/[2U_s - \hbar\delta]$. Due to the exponential divergency, we find that S_0 is always unstable.

[1] B. Josephson, Physics Letters **1**, 251 (1962).
[2] S. Shapiro, Phys. Rev. Lett. **11**, 80 (1963).
[3] G. P. A. Barone, *Physics and Applications of the Josephson Effect* (John Wiley and Sons, New York, 1982).
[4] R. L. Kautz, Reports on Progress in Physics **59**, 935 (1996).
[5] S. V. Pereverzev, A. Loshak, S. Backhaus, J. C. Davis, and R. E. Packard, Nature **388**, 449 (1997).
[6] O. Avenel, Y. Mukharsky, and E. Varoquaux, Nature **397**, 484 (1999).
[7] R. W. Simmonds, A. Marchenkov, J. C. Davis, and R. E. Packard, Phys. Rev. Lett. **87**, 035301 (2001).
[8] K. Sukhatme, Y. Mukharsky, T. Chui, and D. Pearson, Nature **411**, 280 (2001).
[9] D. Sarchi, I. Carusotto, M. Wouters, and V. Savona, Phys. Rev. B **77**, 125324 (2008).

[10] I. A. Shelykh, D. D. Solnyshkov, G. Pavlovic, and G. Malpuech, Phys. Rev. B **78**, 041302 (2008).

[11] M. Abbarchi, A. Amo, V. Sala, D. Solnyshkov, H. Flayac, L. Ferrier, I. Sagnes, E. Galopin, A. Lemaitre, G. Malpuech, and J. Bloch, Nature Physics **09**, 275 (2013).

[12] M. Albiez, R. Gati, J. Fölling, S. Hunsmann, M. Cristiani, and M. K. Oberthaler, Phys. Rev. Lett. **95**, 010402 (2005).

[13] S. Levy, E. Lahoud, I. Shomroni, and J. Steinhauer, Nature **449**, 579 (2007).

[14] L. J. LeBlanc, A. B. Bardon, J. McKeever, M. H. T. Extavour, D. Jervis, J. H. Thywissen, F. Piazza, and A. Smerzi, Phys. Rev. Lett. **106**, 025302 (2011).

[15] C. Ryu, P. W. Blackburn, A. A. Blinova, and M. G. Boshier, Phys. Rev. Lett. **111**, 205301 (2013).

[16] G. Valtolina, A. Burchianti, A. Amico, E. Neri, K. Xhani, J. A. Seman, A. Trombettoni, A. Smerzi, M. Zaccanti, M. Inguscio, and G. Roati, Science **350**, 1505 (2015).

[17] M. Pigneur, T. Berrada, M. Bonneau, T. Schumm, E. Demler, and J. Schmiedmayer, Phys. Rev. Lett. **120**, 173601 (2018).

[18] A. J. Leggett, Rev. Mod. Phys. **73**, 307 (2001).

[19] D. M. Stamper-Kurn and M. Ueda, Rev. Mod. Phys. **85**, 1191 (2013).

[20] C. K. Law, H. Pu, and N. P. Bigelow, Phys. Rev. Lett. **81**, 5257 (1998).

[21] W. Zhang, D. L. Zhou, M.-S. Chang, M. S. Chapman, and L. You, Phys. Rev. A **72**, 013602 (2005).

[22] M.-S. Chang, Q. Qin, W. Zhang, L. You, and M. S. Chapman, Nature Physics **1**, 111 (2005).

[23] J. Kronjäger, C. Becker, M. Brinkmann, R. Walser, P. Navez, K. Bongs, and K. Sengstock, Phys. Rev. A **72**, 063619 (2005).

[24] J. Kronjäger, C. Becker, P. Navez, K. Bongs, and K. Sengstock, Phys. Rev. Lett. **97**, 110404 (2006).

[25] A. T. Black, E. Gomez, L. D. Turner, S. Jung, and P. D. Lett, Phys. Rev. Lett. **99**, 070403 (2007).

[26] Y. Liu, E. Gomez, S. E. Maxwell, L. D. Turner, E. Tiesinga, and P. D. Lett, Phys. Rev. Lett. **102**, 225301 (2009).

[27] C. Klempt, O. Topic, G. Gebreyesus, M. Scherer, T. Henninger, P. Hyllus, W. Ertmer, L. Santos, and J. J. Arlt, Phys. Rev. Lett. **103**, 195302 (2009).

[28] C. Klempt, O. Topic, G. Gebreyesus, M. Scherer, T. Henninger, P. Hyllus, W. Ertmer, L. Santos, and J. J. Arlt, Phys. Rev. Lett. **104**, 195303 (2010).

[29] B. Lücke, M. Scherer, J. Kruse, L. Pezzé, F. Deuretzbacher, P. Hyllus, O. Topic, J. Peise, W. Ertmer, J. Arlt, L. Santos, A. Smerzi, and C. Klempt, Science **334**, 773 (2011).

[30] C. D. Hamley, C. S. Gerving, T. M. Hoang, E. M. Bookjans, and M. S. Chapman, Nat. Phys. **8**, 305 (2012).

[31] D. Linnemann, H. Strobel, W. Muessel, J. Schulz, R. J. Lewis-Swan, K. V. Kheruntsyan, and M. K. Oberthaler, Phys. Rev. Lett. **117**, 013001 (2016).

[32] X.-Y. Luo, Y.-Q. Zou, L.-N. Wu, Q. Liu, M.-F. Han, M. K. Tey, and L. You, Science **355**, 620 (2017).

[33] T. M. Hoang, C. S. Gerving, B. J. Land, M. Anquez, C. D. Hamley, and M. S. Chapman, Phys. Rev. Lett. **111**, 090403 (2013).

[34] T. M. Hoang, M. Anquez, B. A. Robbins, X. Y. Yang, B. J. Land, C. D. Hamley, and M. S. Chapman, Nature Communications **7**, 11233 (2016).

[35] P. L. Kapitza, Soviet Phys. JETP **21**, 588–592 (1951).

[36] L. D. Landau and E. M. Lifshitz, *Mechanics*, 1st ed., Vol. 1 (Pergamon Press, 1960).

[37] R. Citro, E. G. D. Torre, L. D'Alessio, A. Polkovnikov, M. Babadi, T. Oka, and E. Demler, Annals of Physics **360**, 694 (2015).

[38] M. Rigol, V. Dunjko, and M. Olshanii, Nature **452**, 854 (2008).

[39] A. Polkovnikov, K. Sengupta, A. Silva, and M. Vengalattore, Rev. Mod. Phys. **83**, 863 (2011).

[40] J. Eisert, M. Friesdorf, and C. Gogolin, Nature Physics **11**, 124 (2015).

[41] A. Lazarides, A. Das, and R. Moessner, Phys. Rev. E **90**, 012110 (2014).

[42] L. D'Alessio and M. Rigol, Phys. Rev. X **4**, 041048 (2014).

[43] F. Peronaci, M. Schiró, and O. Parcollet, Phys. Rev. Lett. **120**, 197601 (2018).

[44] T. Mori, T. Kuwahara, and K. Saito, Phys. Rev. Lett. **116**, 120401 (2016).

[45] D. A. Abanin, W. De Roeck, W. W. Ho, and F. m. c. Huveneers, Phys. Rev. B **95**, 014112 (2017).

[46] T. Mori, "Floquet prethermalization in periodically driven classical spin systems," arXiv:1804.02165 (2018).

[47] The single-mode spin Hamiltonian has a bounded spectrum, but only describes the low-energy sector of the full Hilbert space.

[48] T. Lahaye, C. Menotti, L. Santos, M. Lewenstein, and T. Pfau, Reports on Progress in Physics **72**, 126401 (2009).

[49] S. Yi, O. E. Müstecaplıoğlu, C. P. Sun, and L. You, Phys. Rev. A **66**, 011601 (2002).

[50] R. Barnett, J. D. Sau, and S. Das Sarma, Phys. Rev. A **82**, 031602 (2010).

[51] Y. Kawaguchi and M. Ueda, Physics Reports **520**, 253 (2012).

[52] S. Knoop, T. Schuster, R. Scelle, A. Trautmann, J. Appmeier, M. K. Oberthaler, E. Tiesinga, and E. Tiemann, Phys. Rev. A **83**, 042704 (2011).

[53] T.-L. Ho, Phys. Rev. Lett. **81**, 742 (1998).

[54] D. Jacob, L. Shao, V. Corre, T. Zibold, L. De Sarlo, E. Mimoun, J. Dalibard, and F. Gerbier, Phys. Rev. A **86**, 061601 (2012).

[55] T. Zibold, V. Corre, C. Frapolli, A. Invernizzi, J. Dalibard, and F. Gerbier, Phys. Rev. A **93**, 023614 (2016).

[56] M. Ueda, Phys. Rev. A **63**, 013601 (2000).

[57] S. Uchino, M. Kobayashi, and M. Ueda, Phys. Rev. A **81**, 063632 (2010).

[58] S. Kohler and F. Sols, New Journal of Physics **5**, 94 (2003).

[59] The steady state population slightly changes over time due to atom losses and/or evaporation of thermal atoms, that change the condensed atom number and thereby U_s (see Fig. 4). The time scale for these changes is very slow (around 10 s) and modifies significantly U_s from its initial value only after very long times (by about 17 % in 10 s), much longer than the typical time-scales for the dynamics. We therefore discard these changes for the discussion in the main text.

[60] S. H. Strogatz, *Nonlinear Dynamics And Chaos*, edited by Addison-Wesley (1994).

[61] A. Eckardt, Rev. Mod. Phys. **89**, 011004 (2017).

[62] L. W. Clark, A. Gaj, L. Feng, and C. Chin, Nature **551**, 356 (2017).

[63] J. Cheng, Phys. Rev. A **81**, 023619 (2010).

[64] J. Kronjäger, K. Sengstock, and K. Bongs, New Journal of Physics **10**, 045028 (2008).

[65] C. Gross, H. Strobel, E. Nicklas, T. Zibold, N. Bar-Gill, G. Kurizki, and M. K. Oberthaler, Nature **480**, 219 (2011).

[66] Y.-Q. Zou, L.-N. Wu, Q. Liu, X.-Y. Luo, S.-F. Guo, J.-H. Cao, M. K. Tey, and L. You, Proceedings of the National Academy of Sciences (2018), 10.1073/pnas.1715105115.

[67] J. P. Wrubel, A. Schwettmann, D. P. Fahey, Z. Glassman, H. K. Pechkis, P. F. Griffin, R. Barnett, E. Tiesinga, and P. D. Lett, Phys. Rev. A **98**, 023620 (2018).